Decomposition of the Multimodal Multidirectional M_2 Internal Tide Field

ZHONGXIANG ZHAO

Applied Physics Laboratory, University of Washington, Seattle, Washington

JINBO WANG, DIMITRIS MENEMENLIS, AND LEE-LUENG FU

Jet Propulsion Laboratory, California Institute of Technology, Pasadena, California

SHUIMING CHEN AND BO QIU

Department of Oceanography, University of Hawai'i at Mānoa, Honolulu, Hawaii

(Manuscript received 2 February 2019, in final form 9 April 2019)

ABSTRACT

The M_2 internal tide field contains waves of various baroclinic modes and various horizontal propagation directions. This paper presents a technique for decomposing the sea surface height (SSH) field of the multimodal multidirectional internal tide. The technique consists of two steps: first, different baroclinic modes are decomposed by two-dimensional (2D) spatial filtering, utilizing their different horizontal wavelengths; second, multidirectional waves in each mode are decomposed by 2D plane wave analysis. The decomposition technique is demonstrated using the M_2 internal tide field simulated by the MITgcm. This paper focuses on a region lying off the U.S. West Coast ranging 20°–50°N, 220°–245°E. The lowest three baroclinic modes are separately resolved from the internal tide field; each mode is further decomposed into five waves of arbitrary propagation directions in the horizontal. The decomposed fields yield unprecedented details on the internal tide's generation and propagation, which cannot be observed in the harmonically fitted field. The results reveal that the mode-1 M_2 internal tide in the study region is dominantly from the Hawaiian Ridge to the west but also generated locally at the Mendocino Ridge and continental slope. The mode-2 and mode-3 M_2 internal tides are generated at isolated seamounts, as well as at the Mendocino Ridge and continental slope. The Mendocino Ridge radiates both southbound and northbound M_2 internal tides for all three modes. Their propagation distances decrease with increasing mode number: mode-1 waves can travel over 2000 km, while mode-3 waves can only be tracked for 300 km. The decomposition technique may be extended to other tidal constituents and to the global ocean.

1. Introduction

The global internal tide field is a multiconstituent multimodal multidirectional field. In the frequency domain, the internal tide field contains a number of semidiurnal and diurnal tidal constituents (K_1, O_1, P_1, Q_1, M_2, S_2, N_2, and K_2), which can be separately extracted from sufficiently long time series of numerical simulations and observations. In this paper, we focus on the dominant M_2 internal tide. Furthermore, each tidal constituent contains multiple baroclinic modes and multiple waves of different horizontal propagation directions. In the continuously stratified ocean, the M_2 internal tide is a sum of orthogonal baroclinic modes (Wunsch 1975; Munk 1981), which are determined by the ocean stratification profile and ocean depth (see details in section 2). In the horizontal, each baroclinic mode contains multiple waves of arbitrary propagation directions, because of their numerous generation sites (Egbert and Ray 2000, 2001) and long-range propagation distances (e.g., Ray and Zaron 2016; Zhao et al. 2016; Zaron 2019). Therefore, the global internal tide field contains waves of different tidal constituents, different baroclinic modes, and different propagation directions. The multiwave interference makes it difficult to track the generation and propagation of individual waves.

It is desirable to decompose the internal tide field into a series of components of different modes and different

Corresponding author: Zhongxiang Zhao, zzhao@apl.uw.edu

DOI: 10.1175/JTECH-D-19-0022.1

directions. First, the internal tide has a mode-dependent transfer function, which is used to calculate depth-integrated energy flux from altimeter-observed sea surface height (SSH) amplitude (Wunsch 2013; Zhao et al. 2016). Therefore, to better observe internal tides by satellite altimetry, it is important to separately resolve waves of different baroclinic modes. Second, the baroclinic modes may have different degrees of coherence during their long-range propagation, because of their different vertical structures and horizontal propagation velocities (Rainville and Pinkel 2006; Ponte and Klein 2015). It is thus necessary to study the coherence of internal tides mode by mode. Third, the baroclinic modes have very different geographic patterns of generation, propagation, and dissipation (Zhao 2018). It is exciting to track individual internal tidal waves to better quantify the global internal tide field. In summary, the decomposed internal tide fields may reveal more information and thus improve our understanding of internal tide dynamics and tide-induced ocean mixing.

Previous studies have shown that plane wave analysis is able to decompose internal waves of different directions (Zhao 2016, 2017a, 2018). By this method, the dominant mode-1 M_2 internal tide has been observed using satellite altimeter data. However, plane wave analysis cannot separate internal waves of different modes. In this paper, we present a new technique that combines plane wave analysis and two-dimensional (2D) spatial filtering. First, we decompose different baroclinic modes by 2D spatial filtering, utilizing their different wavelengths. Second, we decompose each mode into five waves of arbitrary propagation directions by plane wave analysis. The combination of these two methods makes a practical technique of decomposing the multimodal multidirectional internal tide field. By this new decomposition technique, the M_2 internal tide is decomposed into a series of wave components, which reveal features of the internal tide field with unprecedented detail.

This decomposition technique will be demonstrated using the M_2 internal tide field simulated by the Massachusetts Institute of Technology General Circulation Model (MITgcm; Marshall et al. 1997). The MITgcm driven by atmospheric forcing and tidal potential can simultaneously simulate large-scale ocean circulations, mesoscale eddies, submesoscale processes, and internal gravity waves (Rocha et al. 2016a,b; Torres et al. 2018; Qiu et al. 2018; Wang et al. 2018). The MITgcm simulation has been used to study submesoscale processes and their spatiotemporal variations (Rocha et al. 2016a,b; Su et al. 2018). Recently, Savage et al. (2017) studied internal tides simulated by the MITgcm. They reported that the MITgcm-simulated internal tides agree well with those simulated using the Hybrid Coordinate Ocean Model (HYCOM; Arbic et al. 2010; Buijsman et al. 2017) and in situ measurements. Savage et al. (2017) also calculated the frequency–horizontal wavenumber spectra of SSH signals of the MITgcm-simulated internal tides and found that the MITgcm can catch at least the lowest three baroclinic modes. Meanwhile, the MITgcm simulation has been used to examine the partition of balanced motions and unbalanced internal gravity waves (Qiu et al. 2018; Torres et al. 2018). These studies show that the MITgcm simulation contains rich information on internal tides and submesoscale eddies. We are inspired to further explore the internal tides simulated by the MITgcm, with a goal of decomposing the multiwave internal tide field. The decomposed components enable us to better study the generation and propagation of internal tidal waves and thus map their spatial energetics and dissipation. It may be useful in the partition of balanced motions and unbalanced internal waves, which is still challenging question for the upcoming Surface Water and Ocean Topography (SWOT) mission (Fu and Ubelmann 2014; Qiu et al. 2018).

This paper focuses on the region of the California Current System: 20°–50°N, 220°–245°E. This region is particularly interesting for the following reasons. First, the outcome may be useful for the upcoming SWOT calibration–validation experiment (Wang et al. 2018). Second, this region contains a variety of bottom topographic features, including submarine ridges, isolated seamounts, and continental slope (Zhao 2018).

This paper is arranged as follows. In section 2, we briefly describe baroclinic modes and their horizontal propagation velocities. In section 3, we describe the MITgcm-simulated M_2 internal tide field and show its multiwave structure. In section 4, we give a detailed description of our decomposition technique and apply it to the region off the U.S. West Coast. In section 5, we present new features revealed by the decomposed wave components. In the end, we summarize this study in section 6 and discuss future work in section 7.

2. Internal tide baroclinic modes

In this section, we calculate theoretical wavelengths of the lowest four baroclinic modes to examine whether these baroclinic modes are separable by spatial filtering. The theoretical values also provide parameters for our decomposition technique in this paper. Our calculation is based on ocean stratification profiles from

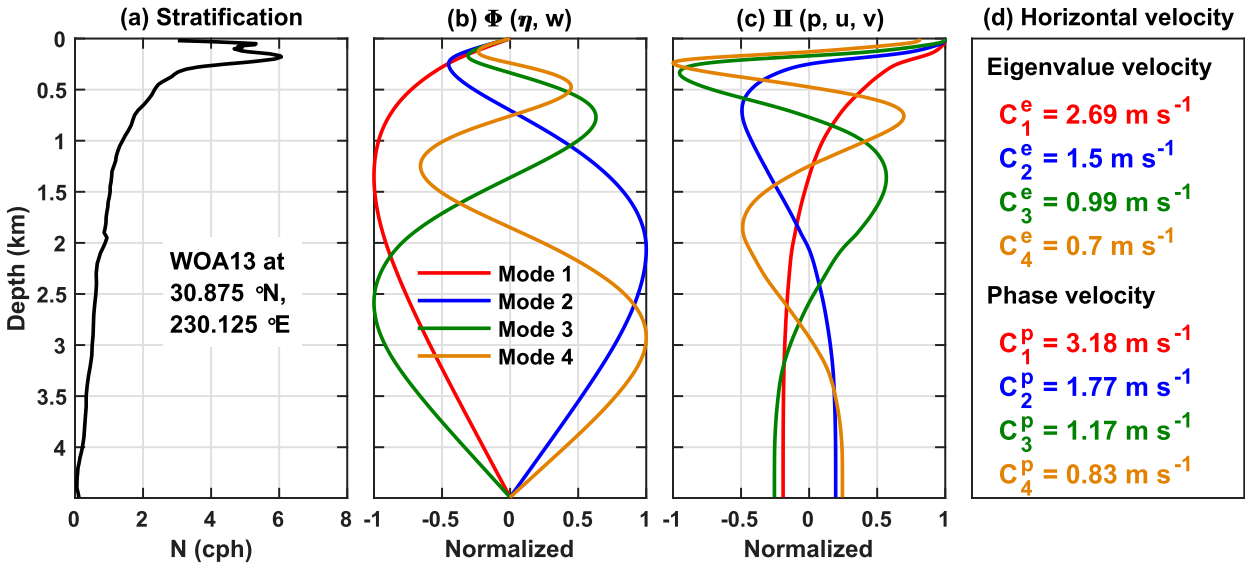

FIG. 1. Stratification profile and baroclinic modes solved from the eigenvalue equation. (a) A stratification profile at 30.875°N, 230.125°E from the *World Ocean Atlas 2013*. (b) Modal structures for displacement η and vertical velocity w. (c) Modal structures for pressure p and horizontal velocity u and v. (d) Eigenvalue and phase velocities of the mode-1–4 M_2 internal tides.

the climatological annual-mean hydrographic data in the *World Ocean Atlas 2013* (*WOA13*; Locarnini et al. 2013; Zweng et al. 2013). Assuming that the ocean bottom is flat, an internal tide in the stratified ocean can be expressed using orthogonal baroclinic modes (Wunsch 1975; Kelly et al. 2012). Each mode has a characteristic vertical structure and freely propagates in the horizontal like a wave in a homogeneous fluid. Assuming that $\Phi(z)$ describes the vertical structures of displacement η and vertical velocity w, the baroclinic modes $\Phi(z)$ can be obtained by the eigenvalue equation (Wunsch 1975; Munk 1981)

$$\frac{d^2\Phi(z)}{dz^2} + \frac{N^2(z)}{c^2}\Phi(z) = 0, \tag{1}$$

subject to the boundary conditions $\Phi(0) = \Phi(-H) = 0$, where H is the ocean depth, $N(z)$ the buoyancy frequency profile, and c the eigenvalue velocity. Assuming $\Pi(z)$ describes the vertical structures of baroclinic pressure p and horizontal velocity u and v, $\Phi(z)$ and $\Pi(z)$ are related via

$$\Pi(z) = \rho_0 c^2 \frac{d\Phi(z)}{dz} \tag{2}$$

and

$$\Phi(z) = -\frac{1}{N^2(z)\rho_0}\frac{d\Pi(z)}{dz}, \tag{3}$$

where ρ_0 is a reference water density.

The eigenvalue velocity c is the phase velocity in a nonrotating fluid. Under the influence of Earth's rotation Ω, the dispersion relation is

$$\omega^2 = K^2c^2 + f^2, \tag{4}$$

where $f\,[\equiv 2\Omega\sin(\text{latitude})]$ is the inertial frequency and K the horizontal wavenumber. The phase velocity c_p can be derived from c following

$$c_p = \frac{\omega}{(\omega^2 - f^2)^{1/2}}c, \tag{5}$$

where ω and f are the tidal and inertial frequencies, respectively. As an example, Fig. 1 gives the buoyancy frequency profile around 31°N, 230°E. A set of baroclinic modes and their corresponding eigenvalues are obtained from Eq. (1). The normalized $\Pi(z)$ and $\Phi(z)$ of the lowest four baroclinic modes are shown in Figs. 1b and 1c, respectively. Figure 1d lists their eigenvalue and phase velocities. This example shows that these baroclinic modes have different vertical structures and different horizontal wavelengths.

Figure 2 shows regional maps of wavelengths of the lowest four baroclinic modes in the range 20°–50°N, 220°–245°E. Figures 2a–d give the mode-1–4 wavelengths, respectively. They have similar spatial patterns, which are mainly determined by ocean depth, ocean stratification, and latitude. We further calculate the ratios of wavelengths of two neighboring modes at each grid point. Figures 2e–g give the histograms of the

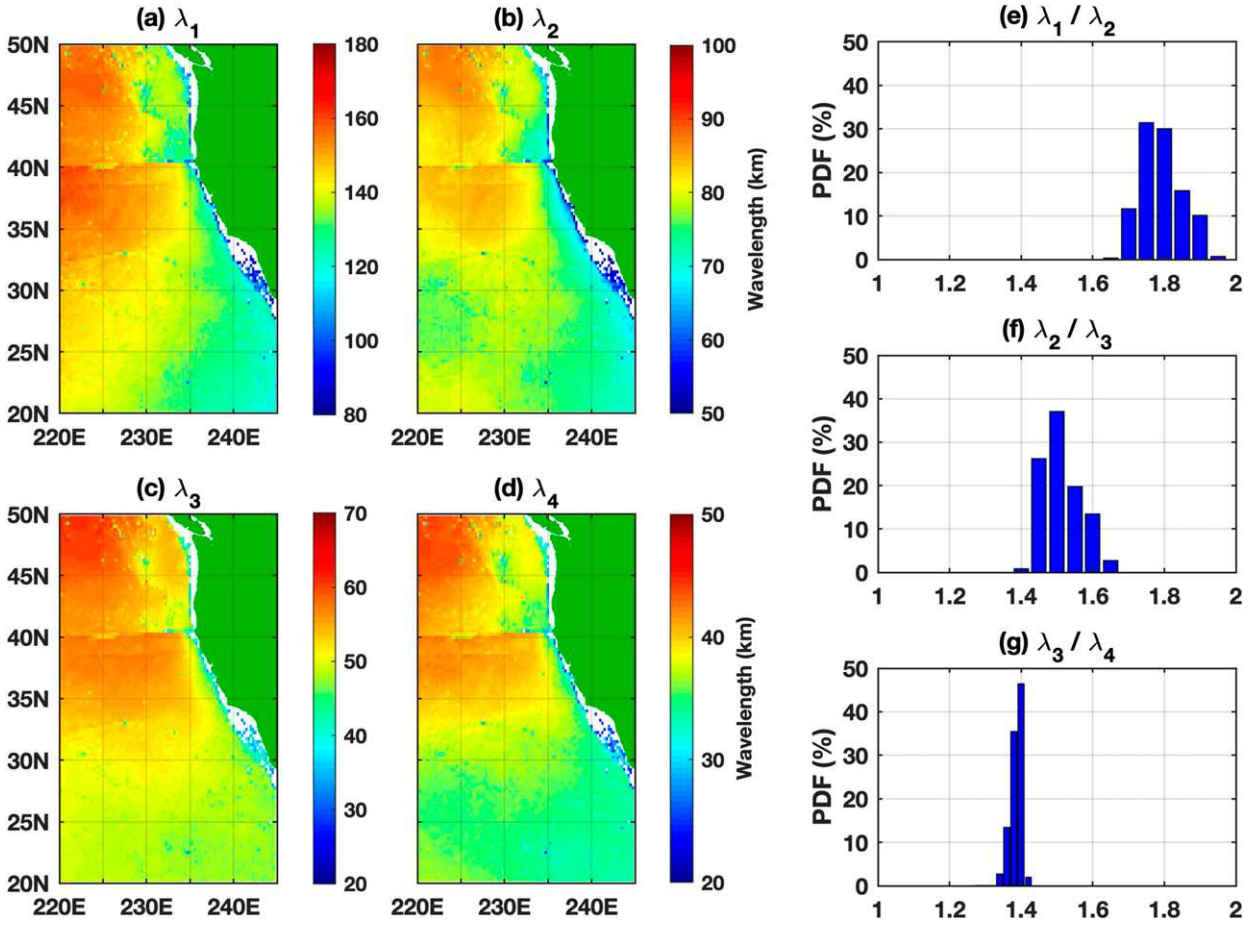

FIG. 2. Wavelengths (km) and ratios of wavelengths (λ_n and K_n denote the nth-mode wavelength and wavenumber, respectively). (left) Wavelengths of the (a) mode-1, (b) mode-2, (c) mode-3, and (d) mode-4 M_2 internal tides, calculated using climatological annual-mean stratification profiles in the *World Ocean Atlas 2013*. (right) Histograms of ratios of wavelengths (i.e., inverse ratios of wavenumbers): (e) λ_1/λ_2 ($\equiv K_2/K_1$), (f) λ_2/λ_3 ($\equiv K_3/K_2$), and (g) λ_3/λ_4 ($\equiv K_4/K_3$). The results show that different baroclinic modes can be separated using their different wavenumbers (wavelengths).

ratios of λ_1/λ_2, λ_2/λ_3, and λ_3/λ_4, respectively, where λ_n denotes the nth-mode wavelength. The ratios concentrate around 1.8, 1.5, and 1.4, respectively. The histograms suggest that these baroclinic modes can be separated by spatial filtering. The theoretical values will be used to determine the cutoff wavenumbers employed in this paper (section 4a).

3. MITgcm-simulated internal tides

The MITgcm run (llc4320) has 1/48° horizontal resolution and 90 vertical levels. The model is forced by 6-hourly atmospheric reanalysis from the European Centre for Medium-Range Weather Forecasts (ECMWF), which is converted to ocean surface fluxes using the bulk formula in Large and Yeager (2004). The barotropic tidal forcing includes eight short-period constituents (K_1, O_1, P_1, Q_1, M_2, S_2, N_2, and K_2) and eight long-period tidal constituents (M_t, M_f, M_m, M_s, M_f, M_{sa}, M_s, and L_n). The barotropic tidal potential is applied to the model by adding an additional surface pressure field to the atmospheric pressure field. Based on a model-data comparison with the tide gauge at the Harvest platform, the llc4320 barotropic tide can be 12% stronger than reality (M. Mazloff 2018, personal communication). However, this discrepancy does not affect our decomposition of the MITgcm-simulated internal tide field.

The sea surface height η is calculated as the full-depth dynamic height from the MITgcm-simulated variables following (Wang et al. 2018)

$$\eta = -\int_{-H}^{0} \frac{\rho'(z)}{\rho_0} dz, \tag{6}$$

where $\rho'(z)$ is the potential density anomaly calculated from the model temperature and salinity output and

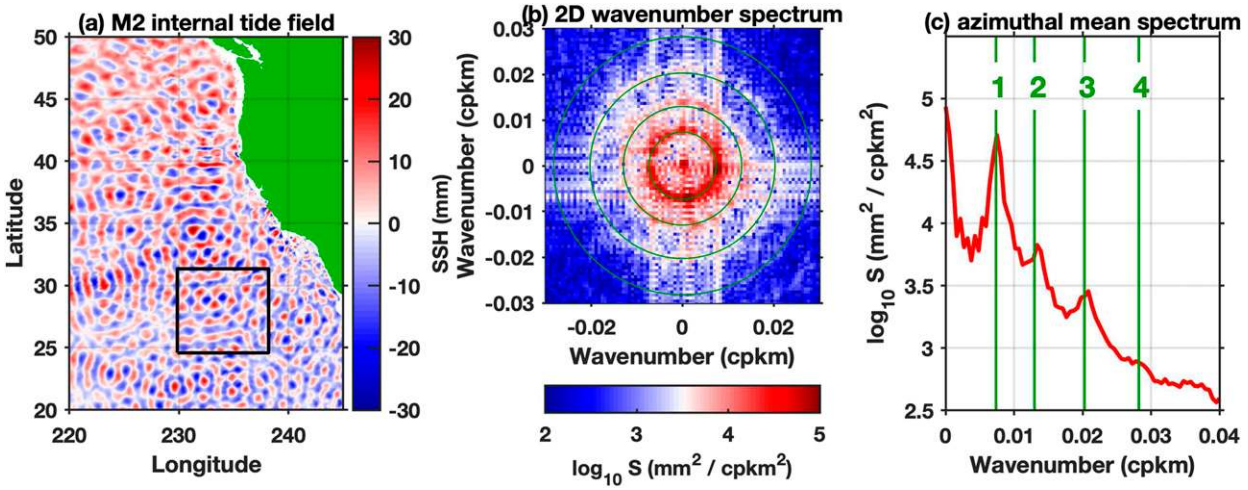

FIG. 3. The MITgcm-simulated M_2 internal tide field and its horizontal 2D wavenumber spectrum. (a) The M_2 internal tide field obtained by harmonic analysis of the MITgcm simulation. (b) The 2D horizontal wavenumber spectrum using the SSH data in the black box in (a), which is about 740 km × 740 km centered at 28°N, 234°E. SSH complex numbers (amplitude and phase) are used in calculating the spectrum. The 2D spectrum shows three concentric rings corresponding to the lowest three baroclinic modes. The green circles mark theoretical wavenumbers in this region from the *World Ocean Atlas 2013*. (c) Azimuthal mean spectrum of (b). The theoretical wavenumbers are marked by vertical green lines and their mode numbers are labeled.

ρ_0 ($\equiv$1027.5 kg m^{-3}) a reference density. The resultant sea surface height gives the steric component caused by baroclinic motions such as internal waves, mesoscale eddies, and thermal expansion.

The model was run for about 14 months from September 2011 to November 2012 and saved hourly snapshots of SSH fields along with other key variables. The year-long MITgcm hourly output is sufficiently long to separate the eight semidiurnal and diurnal tidal constituents. We focus on the M_2 internal tide in this paper. A pointwise harmonic analysis of the hourly output is performed on each grid point using T_Tide to get internal tides (Pawlowicz et al. 2002). The original 1/48° model output is thinned to 1/24° by a four-point-average operator, with a goal of reducing the size of the model output and computation time. It does not affect our study because internal tides have wavelengths of 50–150 km (section 2).

Figure 3 illustrates the MITgcm-simulated M_2 internal tide field and its multimodal multidirectional feature. Figure 3a gives the snapshot M_2 internal tide field obtained by pointwise harmonic analysis of the year-long MITgcm hourly output. Using the SSH data in a window of 740 km × 740 km centered around 28°N, 234°E (Fig. 3a, black box), we calculate the 2D wavenumber spectrum by 2D Fourier transform (see details in section 4a). Figure 3b shows the resultant 2D wavenumber spectrum. It shows several concentric rings. This feature agrees with the 2D wavenumber spectra calculated using the STORMTIDE-simulated (Li et al. 2015) and satellite-observed internal tide fields (Ray and Zaron 2016). Figure 3c shows the azimuthal mean spectrum. It shows three outstanding spectral peaks. The theoretical wavenumbers of the mode-1–4 M_2 internal tides are overlaid in the spectra (Figs. 3b,c, green lines). The good alignment confirms that the MITgcm-derived wavenumbers agree well with the area-median theoretical values from *WOA13* climatological ocean stratification (section 2). This feature also agrees with previously observed frequency–horizontal wavenumber spectra (Savage et al. 2017). It confirms that the MITgcm can catch at least three baroclinic modes. It is worth pointing out that the 2D spectrum is not radially symmetric (Fig. 3b), which suggests the strength variation of internal tides in different propagation directions, as confirmed in our decomposed results (section 5). In summary, Fig. 3 reveals that the MITgcm-simulated internal tide field consists of multimodal multidirectional waves.

4. Methodology

In this paper, we decompose the MITgcm-simulated multimodal multidirectional M_2 internal tide field using a two-step procedure. First, we separate different baroclinic modes by 2D spatial filtering. Second, we decompose each baroclinic mode into multiple waves of arbitrary propagation directions by 2D plane wave analysis. These two steps are described in sections 4a and 4b, respectively. Errors in the decomposition technique are presented in section 4c.

a. Step 1: Decomposition of multiple baroclinic modes

We separate multiple baroclinic modes by 2D spatial filtering. First, we calculate 2D wavenumber spectrum from the MITgcm-simulated SSH field following

$$S(k,l)=\sum_{x=0}^{N-1}\sum_{y=0}^{N-1}\eta(x,y)e^{-i(2\pi/N)(xk+yl)}, \tag{7}$$

where $\eta(x, y)$ is the SSH field of the harmonically fitted M_2 internal tide and k and l are horizontal wavenumbers in the x and y direction, respectively. Note that $\eta(x, y)$ are complex numbers with information about both amplitude and phase. Second, we filter the wavenumber spectrum $S(k, l)$ by 2D spatial filtering in the spectral domain following

$$\tilde{S}(k,l)=\begin{cases}0, & \text{if } K<K_{\rm lb}\\ S(k,l), & \text{if } K_{\rm lb}\le K<K_{\rm ub}\\ 0, & \text{if } K\ge K_{\rm ub}\end{cases}, \tag{8}$$

where $K(\equiv\sqrt{k^2+l^2})$ is the horizontal wavenumber and $K_{\rm lb}$ and $K_{\rm ub}$ are the lower-bound and upper-bound wavenumbers, respectively. Third, the filtered spectrum $\tilde{S}(k, l)$ is converted back to the physical space by inverse Fourier transform

$$\eta^{w}(x,y)=\frac{1}{N^2}\sum_{k=0}^{N-1}\sum_{l=0}^{N-1}\tilde{S}(k,l)e^{i(2\pi/N)(xk+yl)}, \tag{9}$$

where $\tilde{S}(k, l)$ is the 2D filtered wavenumber spectrum and $\eta^{w}(x, y)$ is the resultant map of internal waves.

This method is illustrated in Fig. 4. Figure 4c shows the raw M_2 internal tide field obtained by pointwise harmonic analysis. Here, it is a subregion about 740 km × 740 km centered around 28°N, 234°E. We have converted the SSH map from the longitude–latitude coordinates to the Cartesian coordinates. Its 2D wavenumber spectrum is calculated following Eq. (7) and shown in Fig. 4a. As demonstrated earlier, Fig. 4a shows three concentric rings that correspond to the mode-1–3 M_2 internal tides, respectively. To extract the mode-1 component, the 2D wavenumber spectrum is applied by a 2D bandpass filter as shown in Fig. 4b (blue circular band). As described by Eq. (8), the product of the 2D spectrum and the 2D filter gives the wavenumber spectrum of the mode-1 component. Figure 4d shows the mode-1 M_2 internal tide obtained by inverse Fourier transform following Eq. (9). Following the same procedure, we extract the mode-2 (Fig. 4e) and mode-3 (Fig. 4f) M_2 internal tides. In addition, we also obtain the low-pass-filtered component (Fig. 4g) and high-pass-filtered component (Fig. 4h). Thus, we decompose the raw M_2 internal tide into five components. Note that the ≈100-km boundary of these fields is fouled by artificial wiggles in the 2D spatial filter (Fig. 4, dashed-line boxes). We only keep the inner field inside the dashed-line boxes.

These five components are obtained by the same procedure, but with different cutoff wavenumbers. Specifically, the cutoff wavenumber between modes n and $n + 1$ is $0.5(K_n + K_{n+1})$, where K_n and K_{n+1} are their theoretical wavenumbers, respectively. The cutoff wavenumber is at the central position to better separate two neighboring baroclinic modes. As shown in Fig. 2, these cutoff wavenumbers are clearly away from wavenumber ratios. They are shown as black circles in Figs. 4a and 4b, and listed in Table 1. For example, to obtain the mode-1 component, the lower-bound and upper-bound wavenumbers are $0.5K_1$ and $0.5\ (K_1 + K_2)$, respectively.

We apply the above procedure to our study region ranging 20°–50°N, 220°–245°E. As demonstrated in Fig. 4, this procedure is applied to a number of half-overlapping windows of about 7° longitude × 7° latitude, instead of one 2D spatial filter over the whole region. This strategy is to account for the strong spatial variation of theoretical wavelengths as shown in Fig. 2. For each small window, we determine the area-median theoretical wavenumbers and use them in the 2D spatial filter as described above. In the end, our filtered fields are mosaics of a number of small windows. As shown in section 4c, errors in the multimodal decomposition is only 0.1 mm, compared to the 10-mm internal tide signal.

Figure 5 presents the decomposed multimodal M_2 internal tide fields. The raw M_2 internal tide field is shown in Fig. 5a. The mode-1, mode-2 and mode-3 M_2 internal tides are shown in Figs. 5b–d, respectively. The low-pass- and high-pass-filtered fields are shown in Figs. 5e and 5f, respectively. The sum of the five components (not shown) approximates to the raw internal tide field (Fig. 5a) with very small differences (section 4c). The 3000-m isobaths are shown in these panels. The large-scale spatial variation of the low-pass component implies that it mainly contains barotropic tide residual several millimeters in amplitude. Note that the discontinuity in Fig. 5f is because the presence of nontidal noise and different cutoff wavenumbers are used in these small windows. While the high-pass component mainly contains higher-mode M_2 internal tides (modes ≥4). Importantly, we now separately extract the mode-1, mode-2, and mode-3 M_2 components. The mode-2 and mode-3 SSH amplitudes

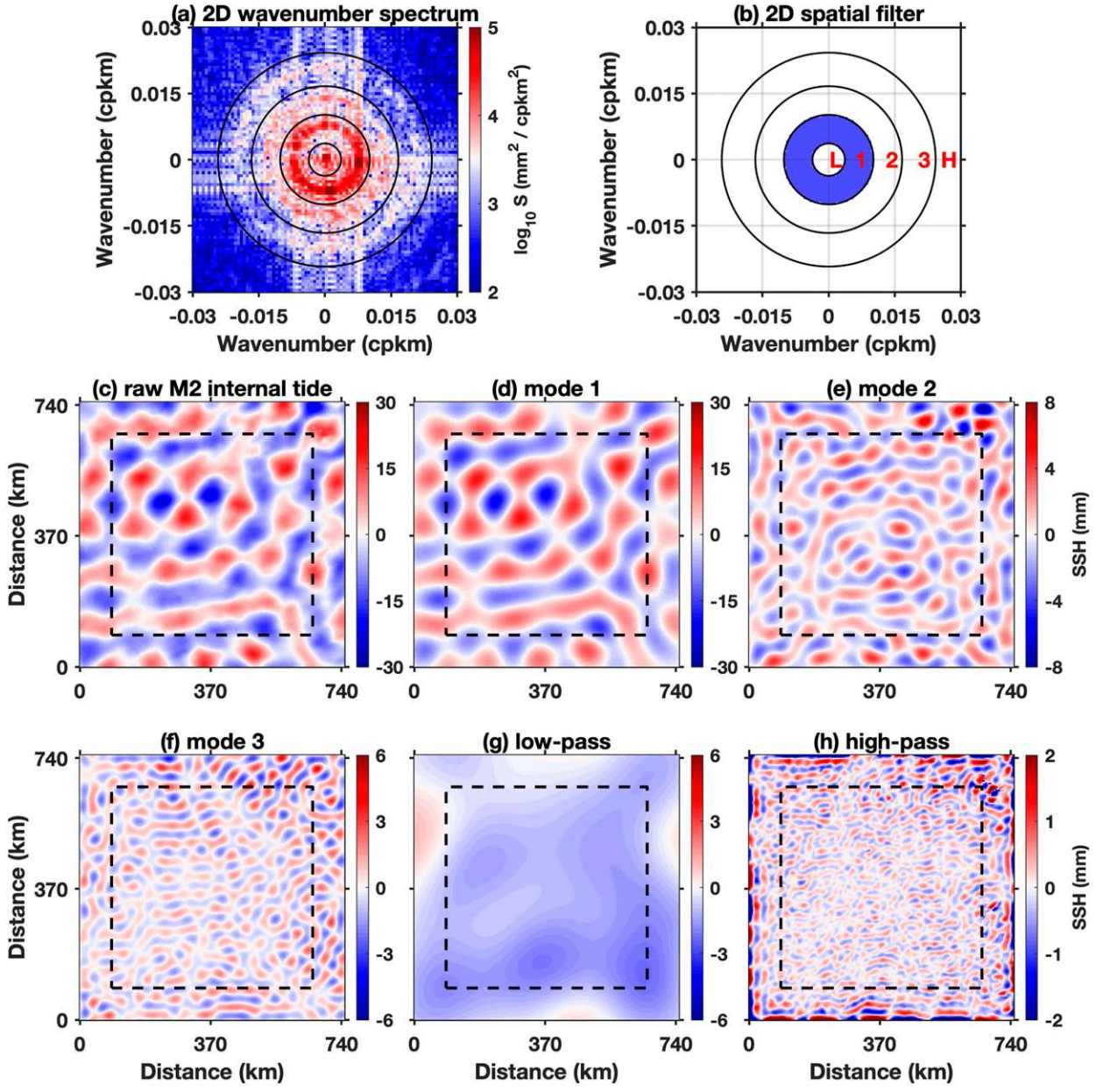

FIG. 4. Decomposition of the M_2 internal tide by 2D spatial filtering. (a) The 2D wavenumber spectrum of the raw M_2 internal tide field [shown in (c)]. SSH complex numbers (amplitude and phase) are used in calculating the spectrum. Black circles mark the cutoff wavenumbers in 2D spatial filtering. Their values are listed in Table 1. (b) The 2D spatial filters with cutoff wavenumbers [shown in (a)]. The blue circular band highlights the 2D filter employed for mode 1. Five components are labeled. (c) The raw M_2 internal tide field centered at 28°N, 234°E (Fig. 3a, box). (d) Mode 1. (e) Mode 2. (f) Mode 3. (g) Low-pass-filtered component. (h) High-pass-filtered component. The ≈100-km boundary of the filtered fields is affected by artificial wiggles and thus discarded.

are lower than 10 mm. In the raw M_2 field (Fig. 5a), they are masked by the dominant mode-1 component, which has SSH amplitudes up to 30 mm (Fig. 5b). The separately resolved fields yield information on the generation and propagation of the internal tide for all three modes. For example, the mode-2 and mode-3 components are dominantly associated with topographic features such as the Mendocino Ridge. However, each of these three modes may contain multiple waves of different propagation directions. The multiwave interference still makes it difficult to track their generation and propagation. In the next step, we decompose each mode into multiple waves of arbitrary propagation directions.

TABLE 1. Cutoff wavenumbers used in the 2D bandpass spatial filter (K_n denotes the nth-mode theoretical M_2 wavenumber).

Component	Cutoff wavenumber	
	Lower bound (K_{lb})	Upper bound (K_{ub})
Low pass	—	$0.5K_1$
Mode 1	$0.5K_1$	$0.5(K_1 + K_2)$
Mode 2	$0.5(K_1 + K_2)$	$0.5(K_2 + K_3)$
Mode 3	$0.5(K_2 + K_3)$	$0.5(K_3 + K_4)$
High pass	$0.5(K_3 + K_4)$	—

b. Step 2: Decomposition of multidirectional waves

In this section, we decompose each of the three modes into multiple waves by 2D plane wave analysis. Plane wave analysis is a variant of harmonic analysis. By this method, internal tidal waves are extracted by fitting plane waves using SSH data at multiple data points in a fitting window. In contrast, pointwise harmonic analysis extracts internal tides using data at one single point. This technique separates internal tidal waves of different propagation directions and thus resolves multiwave interference. This method has been employed to extract M_2, S_2, O_1, and K_1 internal tides from satellite altimetry (Zhao 2014, 2016, 2017a, 2018).

In this study, we reconstruct each baroclinic mode using five waves following

$$\eta(x,y,t) = \sum_{n=1}^{5} A_n \cos(Kx\cos\theta_n + Ky\sin\theta_n - \omega t - \phi_n), \tag{10}$$

where x and y are the east and north in the Cartesian coordinates, t is time, ω is the M_2 frequency, K is the median theoretical M_2 wavenumber within one fitting

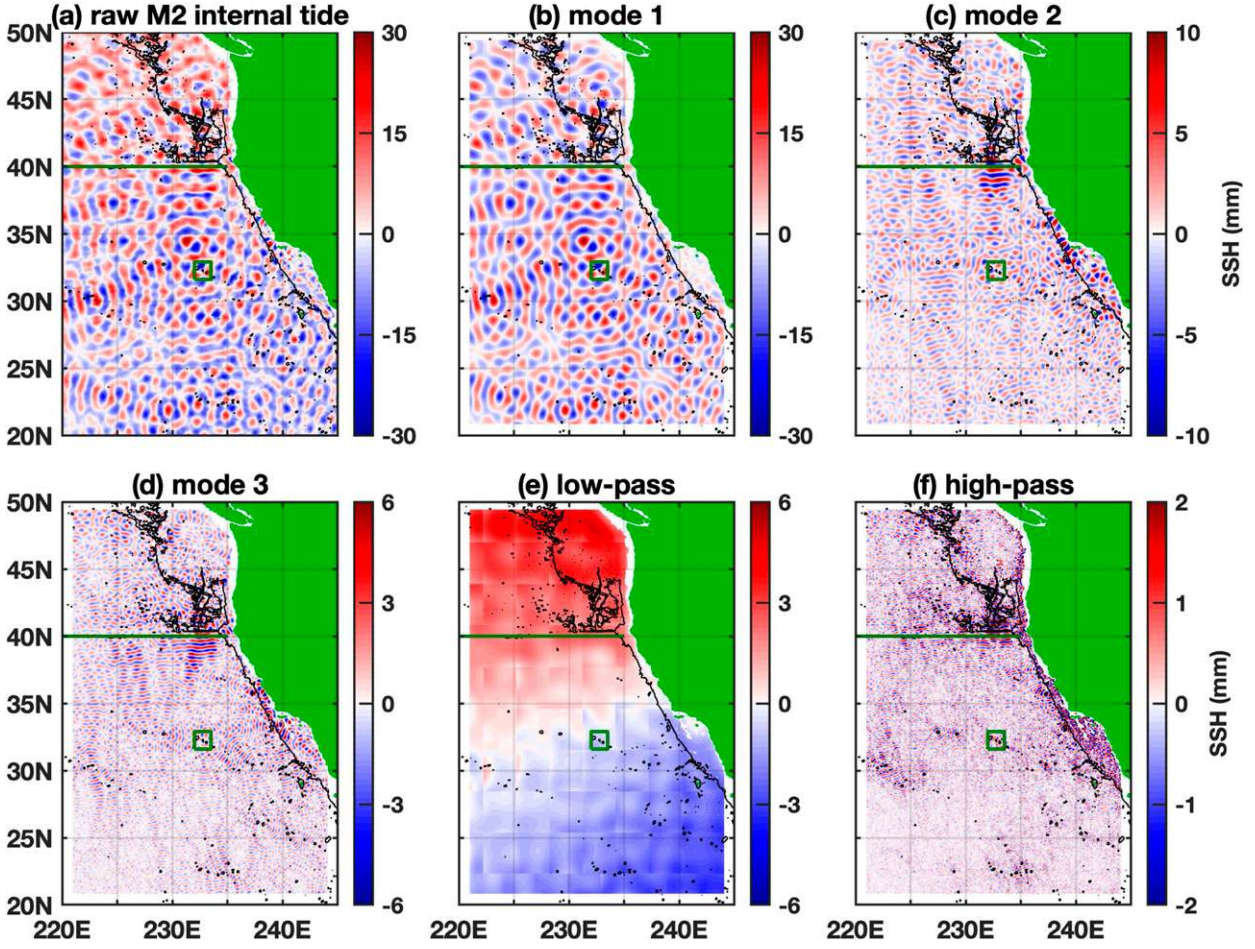

FIG. 5. The M_2 internal tide field is decomposed into five components by 2D spatial filtering. Shown are snapshot internal tide SSH fields in Greenwich phase: (a) the raw M_2 internal tide field from the MITgcm simulation (as in Fig. 3a), (b) mode 1, (c) mode 2, (d) mode 3, (e) low-pass-filtered component (barotropic tide residual), and (f) high-pass-filtered component (modes ≥4). The 3000-m isobaths are shown in black. The sum of the five components equals to the raw M_2 internal tide field. The Mendocino Ridge and Fieberling Seamount are indicated using green lines and boxes, respectively.

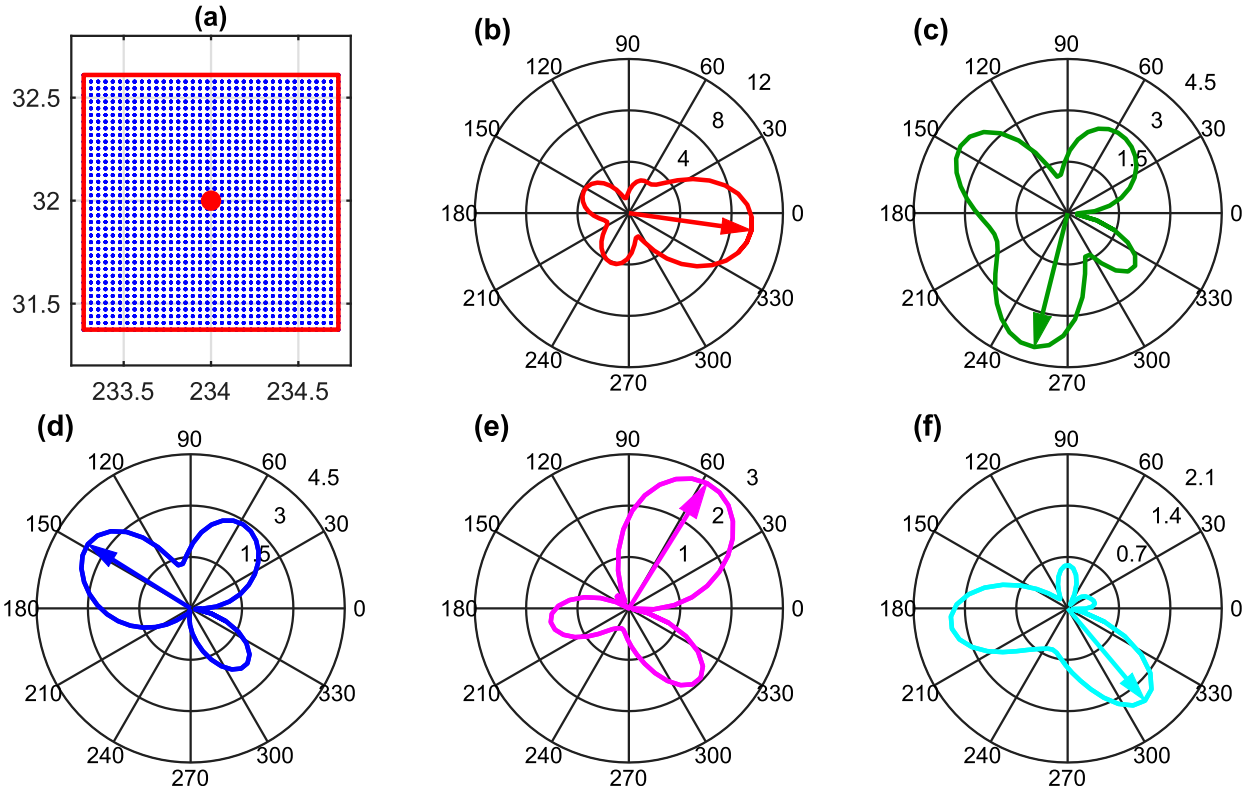

FIG. 6. Decomposition of the mode-1 M_2 internal tide field by plane wave analysis. (a) Data points in a 140 km × 140 km fitting window centered at 32°N, 234°E. There are 1404 data points in this fitting window. (b) Sea surface height (SSH) amplitude (mm) vs direction obtained by fitting a plane wave in each compass direction. The first mode-1 M_2 internal tidal wave (red arrow) is determined from the largest lobe. After removing the first wave, this procedure is repeated to determine the (c) second, (d) third, (e) fourth, and (f) fifth waves.

window, and A_n, θ_n, and ϕ_n are the amplitudes, horizontal directions, and phases of the five waves. They are determined by least squares fits using all SSH data in a fitting window.

An iteration method has been developed to extract an arbitrary number of waves. Figure 6 gives an example to demonstrate how to determine five mode-1 M_2 internal tidal waves at 32°N, 234°E. Figure 6a shows all data points in a fitting window of 140 km × 140 km. Here, 140 km is chosen, because it is about one wavelength in this region. In each compass direction (with 3° angular increment), the amplitude and phase of one plane wave are determined by the least squares fit. When the resultant amplitudes are plotted with respect to direction in polar coordinates, an internal tidal wave appears as a lobe (Fig. 6b). The amplitude, phase, and direction of the first mode-1 wave are thus determined from the largest lobe (red arrow). The SSH signal of the determined wave is predicted and removed from the initial SSH data. This step removes both the internal wave itself and its side lobes. This procedure can be repeated to extract an arbitrary number of waves. Here, it is conducted five times to extract five mode-1 internal tidal waves. Then each wave is refitted with other four waves temporarily removed to reduce wave–wave interference. In the end, five mode-1 M_2 internal tidal waves are obtained, and their vector superposition gives the mode-1 M_2 internal tide solution at 32°N, 234°E. Errors in the plane wave analysis method will be studied in section 4c.

The regional mode-1 M_2 internal tide field is decomposed using the 2D plane wave analysis method as demonstrated in Fig. 6. All parameters employed are given in Table 2. Our five-wave decomposition is conducted at a regular grid of 0.1° longitude × 0.1° latitude. The decomposition can be validated by the good agreement between the five-wave fitted field and the raw M_2 internal tide field (Figs. 7a,d). The mode-2 and mode-3 M_2 internal tides are decomposed following the same procedure but with different parameters (Table 2). First of all, the three baroclinic modes have very different wavenumbers (section 2). To separately extract them, K in Eq. (10) must be their respective theoretical wavenumbers, respectively. For modes 2 and 3, the fitting windows are 75 km × 75 km and 50 km × 50 km, respectively. These values are chosen to be one wavelength

TABLE 2. Parameters employed in the decomposition of the mode-1–3 M_2 internal tide fields by 2D plane wave analysis.

Parameter	Mode 1	Mode 2	Mode 3
Longitudinal range	220°–245°E		
Latitudinal range	20°–50°N		
Wavenumber	Theoretical values from *WOA13*		
Spatial grid (°)	0.1	0.05	0.05
Size of fitting windows (km)	140	75	50
Number of fitted waves		5	

for each mode. For both modes, the decomposition is made at 0.05° longitude × 0.05° latitude, which is needed to resolve the relatively shorter mode-2 and mode-3 waves. For both modes, the five-wave fitted results agree with their original results very well (Fig. 7). The good agreements suggest that each baroclinic mode can be accounted for by five waves. The advantage of the five-wave decomposed results is that it can yield more information of the internal tide's generation and propagation.

Figure 8 shows the final decomposed M_2 internal tide components by our two-step decomposition technique. Modes 1–3 each has been decomposed into five waves of arbitrary propagation directions. To better present the decomposed results, we show the five mode-1 internal tidal waves in four directional ranges: the eastbound component contains waves with propagation direction ranging from −45° to 45° (Fig. 8e); the northbound component with propagation direction ranging from 45° to 135° (Fig. 8f); the westbound component with propagation direction ranging from 135° to 225° (Fig. 8g); and the southbound component with propagation direction ranging from 225° to 315° (Fig. 8h). Similarly, we show the four components of the mode-2 M_2 internal tide in

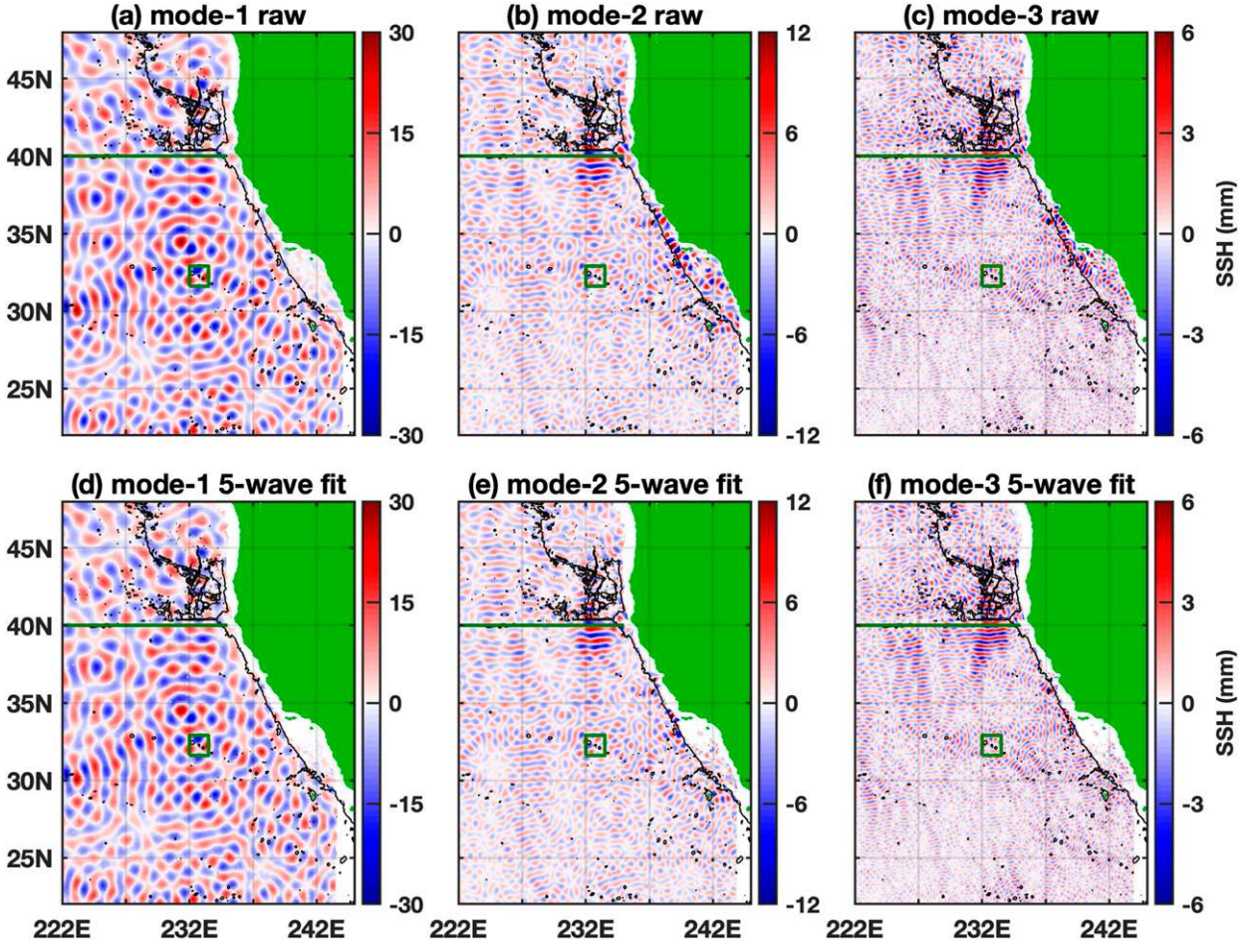

FIG. 7. (top) The mode-1–3 M_2 internal tide fields and (bottom) their respective five-wave reconstructed fields. Shown are snapshot internal tide SSH fields in Greenwich phase. (a) Mode-1 M_2 internal tide field obtained by 2D spatial filtering (as in Fig. 5b). (d) Reconstructed mode-1 M_2 internal tide field using five plane waves. (b),(e) As in (a) and (d), but for the mode-2 M_2 internal tide. (c),(f) As in (a) and (d), but for the mode-3 M_2 internal tide. The Mendocino Ridge and Fieberling Seamount are indicated using green lines and boxes, respectively.

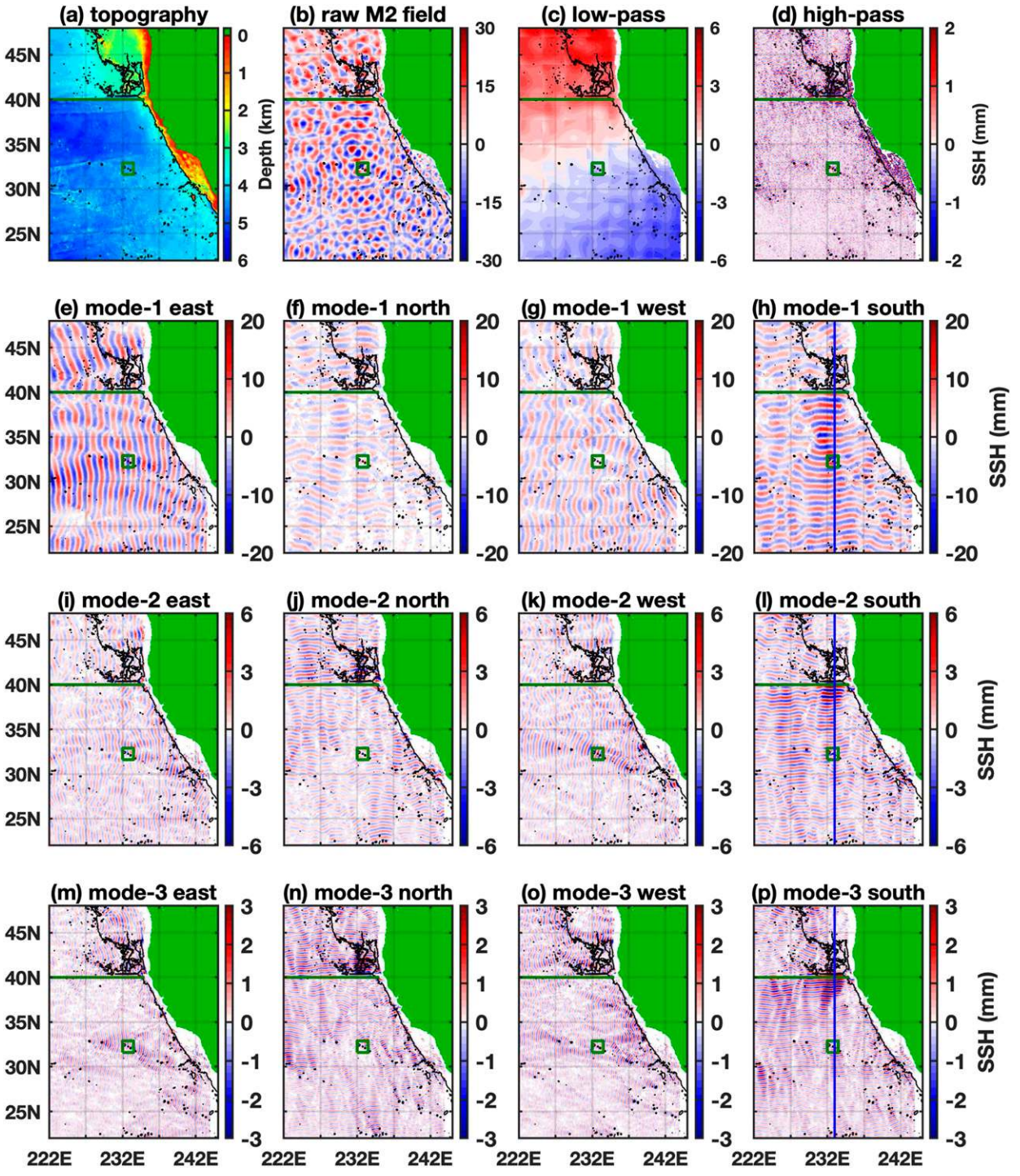

FIG. 8. The raw M_2 internal tide field is decomposed into 14 components by 2D spatial filtering and plane wave analysis. Shown are snapshot internal tide SSH fields in Greenwich phase. (a) Bottom topography. (b) The M_2 internal tide field obtained by harmonic analysis of the MITgcm simulation (as in Fig. 3a). (c) Low-pass-filtered component (as in Fig. 5e). (d) High-pass-filtered component (as in Fig. 5f). (e)–(h) Four decomposed mode-1 internal tide components: eastbound component with propagation direction ranging from –45° to 45°, northbound component ranging from 45° to 135°, westbound component ranging from 135° to 225°, and southbound component ranging from 225°–315°, respectively. (i)–(l) As in (e)–(h), but for the mode-2 M_2 component. (m)–(p) As in (e)–(h), but for the mode-3 M_2 component. In all panels, the 3000-m isobaths are shown in black. The Mendocino Ridge and Fieberling Seamount are indicated using green lines and boxes, respectively. Southbound mode-1–3 components along the blue lines are shown in Fig. 10.

Figs. 8i–l and the mode-3 M_2 internal tide in Figs. 8m–p. Note that the decomposed fields lack output in the boundary region, because there are insufficient SSH data in the plane wave analysis. Figure 8a shows bottom topography to better identify generation sites of the internal tidal waves. For convenience, Figs. 8c and 8d show the low-pass- and high-pass-filtered components, respectively, as in Figs. 5e and 5f. In summary, we have decomposed the raw harmonically fitted M_2 internal tide field (Fig. 8b) into 14 components (Figs. 8c–p).

c. *Errors in the decomposition technique*

Here, we present errors in each step of our decomposition technique. For each decomposition, error ε can be calculated to be the vector difference between an original field and the sum of decomposed fields following

$$\varepsilon = \left| \eta_o e^{i\phi_o} - \sum_n \eta_n e^{i\phi_n} \right|, \tag{11}$$

where η_o and ϕ_o are the amplitude and phase of the original field, η_n and ϕ_n are the amplitudes and phases of a number of decomposed fields, and $|x|$ denotes the absolute value of the complex number.

We first calculate errors in the multimodal decomposition. The original field is the raw M_2 internal tide field obtained by harmonic analysis (one snapshot field is shown in Fig. 5a). The reconstructed field is the sum of five decomposed baroclinic modes, whose snapshots are shown in Figs. 5b–f. The error is calculated using Eq. (11) and shown in Fig. 9a. Figure 9b gives its histogram, showing that the error has an RMS value of 0.1 mm. It is negligibly small compared to the 10-mm SSH signal.

We next calculate errors in the plane wave analysis for all three modes. For mode 1, the original field is the bandpass-filtered mode-1 M_2 internal tide field (one snapshot field is shown in Fig. 7a); the reconstructed field is the sum of five plane wave fitted waves (Fig. 7d). The error map is shown in Fig. 9c, and its histogram is shown in Fig. 9d. Following the same procedure, the errors for modes 2 and 3 are calculated and shown in Figs. 9e–h, respectively. The results show that the RMS errors for modes 1–3 are 1.35, 0.48, and 0.23 mm, respectively. The decrease with increasing mode number is because the signal itself becomes smaller. The errors are because our plane wave analysis has a stricter constraint than pointwise harmonic analysis. It is likely that the errors can be further reduced by extracting more than five waves.

The overall error in our decomposition technique is given in Fig. 9i and 9j. It is the vector difference between the raw harmonically fitted M_2 internal tide (Fig. 8b) and the sum of the 14 decomposed fields (Figs. 8c–p). The RMS error is 1.43 mm, a little larger than 1.35 mm for mode 1 only. Figures 9c and 9i have very similar spatial pattern, suggesting that the error is dominantly from the mode-1 component. Most of the error occurs at topographic features, implying that the internal tide there is more complicated. It is likely due to the coupling among different baroclinic modes (Kelly et al. 2013). Overall, the RMS error of 1.43 mm is much lower than the 10-mm SSH internal tide signal. It shows that our decomposition technique is reliable.

5. Results

a. *Decomposed internal tide fields*

Here, we show that the decomposed fields reveal new information on the internal tide field. Individual internal waves can be observed in the decomposed components shown in Figs. 8e–p, because they are exempt from multiwave interference. Numerous internal tidal beams are observed to radiate from notable topographic features such as the Mendocino Ridge and Fieberling Seamount (Fig. 8a). In particular, because of their relatively narrow beamwidth, mode-2 and mode-3 internal tidal beams are observed to be associated with isolated seamounts. One can see that the internal tidal beams occur on the lee side of topographic features. For example, the eastbound, northbound, westbound, and southbound waves occur to the east, north, west, and south of topographic features, respectively (Figs. 8m–p). It has long been known that internal tides are generated in the tide–topography interaction (Wunsch 1975; Garrett and Kunze 2007). Our decomposition results show well-defined internal tidal beams and their collocation with notable topographic features. These features validate our decomposition technique. In contrast, these internal tidal beams cannot be detected in the raw multiwave interfered field (Fig. 8b).

The decomposed results enable us to better study the generation and propagation of internal tides for all three modes. One can see that mode-1 waves are dominantly eastbound (Fig. 8e), which are actually from the Hawaiian Ridge (outside our study region). The statement has been verified by satellite altimetric results (Ray and Zaron 2016; Zhao et al. 2016). In addition, mode-1 waves are also generated locally at the Mendocino Ridge (Figs. 8f,h) and continental slope (Fig. 8g). The southbound mode-1 M_2 internal tidal waves have been previously observed by in situ measurements (e.g., Althaus et al. 2003; Alford 2010; Musgrave et al. 2017). In contrast, mode-2 and mode-3 internal tidal waves are

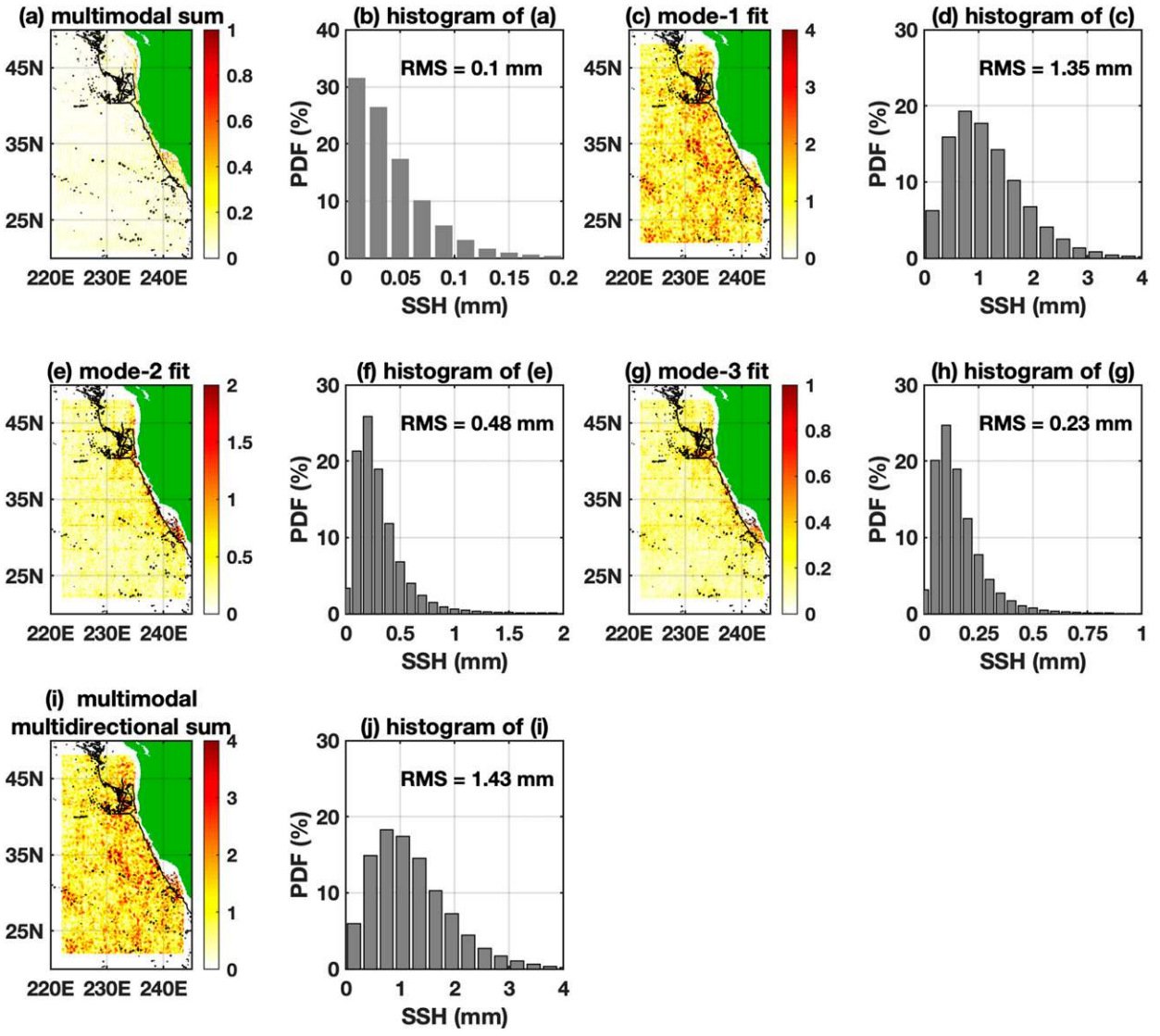

FIG. 9. Errors in the decomposition technique (SSH unit is mm). The 3000-m isobaths are shown in black. (a) Error in the multimodal decomposition, that is, the difference between the raw M_2 internal tide field (Fig. 5a) and the sum of the five decomposed modes shown in Figs. 5b–f. (b) Histogram of (a) (PDF = probability distribution function). (c) Error in the mode-1 plane wave fit, that is, the difference between the bandpass-filtered mode-1 field (Fig. 7a) and the sum of the five plane wave fitted waves (Fig. 7d). (d) Histogram of (c). (e),(f) As in (c) and (d), but for the mode-2 component. (g),(h) As in (c) and (d), but for the mode-3 component. (i) The overall error in the multimodal multidirectional decomposition, that is, the difference between the raw M_2 internal tide field (Fig. 8b) and the sum of the 14 decomposed fields shown in Figs. 8c–p. (j) Histogram of (i).

mainly generated locally at the Mendocino Ridge, isolated seamounts and continental slope. Isolated seamounts (e.g., Fieberling Seamount) radiate both mode-2 and mode-3 in all four directional ranges (Figs. 8i–p). However, isolated seamounts do not seem to generate mode- 1 waves or affect their propagation, which may imply that the relatively larger mode-1 waves are not sensitive to small-scale topographic features. The Mendocino Ridge can generate mode-1, mode-2, and mode-3 M_2 internal tidal waves. In addition, the high-pass component (Fig. 8d) shows wavelike pattern to the south of Mendocino, suggesting that the Mendocino Ridge may generate M_2 internal tides of mode 4 or higher. Our method may be used to further decompose the high-pass component.

b. *Internal tidal beams*

In this section, we exemplify the along-beam information revealed by the decomposed results. The Mendocino Ridge has a west–east orientation and thus

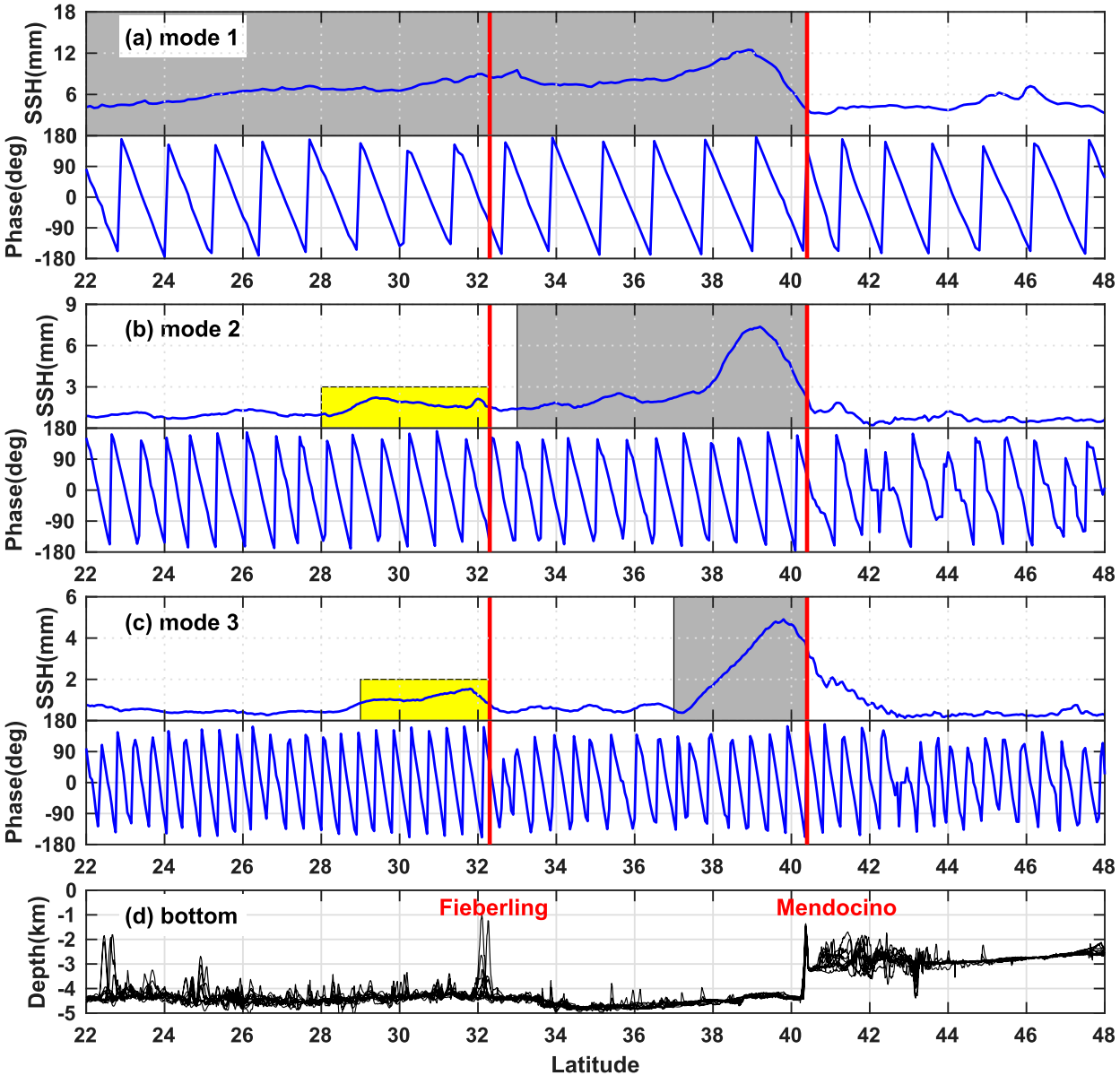

FIG. 10. Amplitudes and phases of the southbound M_2 internal tides: (a) mode 1, (b) mode 2, and (c) mode 3. Shown are the mean values in a 1° stripe within 232.5°–233.5°E. Its central longitude (233°E) is shown as blue lines in Fig. 8. (d) Bottom topography. Two notable topographic features labeled: the Mendocino Ridge and Fieberling Seamount (red text and red vertical lines). Gray boxes in (a)–(c) highlight the Mendocino Ridge–induced internal tides. Yellow boxes in (b) and (c) highlight the Fieberling Seamount–induced internal tides.

radiates southbound and northbound M_2 internal tidal waves (Fig. 8). Here, we examine the southbound mode-1, mode-2, and mode-3 M_2 internal tides from the Mendocino Ridge. Figure 10 shows their amplitudes and phases along 233°E (Fig. 8, blue lines). The along-beam amplitudes and phases are the cross-beam means within the 1° stripe from 232.5° to 233.5°E. Figure 10d shows the along-beam bottom topography. Along this section, two notable features are labeled: the Mendocino Ridge and Fieberling Seamount. Figure 10 shows that the amplitudes are smooth and the phases increase linearly for all three modes. These features further validate our decomposition technique.

The along-beam amplitude and phase contain useful information on their generation and propagation. Along the beam, the maximum amplitudes of mode-2 and mode-3 M_2 internal tides are lower than 8 and 5 mm, respectively, in contrast to the 12-mm amplitudes of

mode 1. The largest SSH amplitudes occur to the south of the Mendocino Ridge (Fig. 10, gray boxes), suggesting that Mendocino is one strong generation source. Fieberling Seamount radiates mode-2 and mode-3 internal tidal waves (Fig. 10, yellow boxes) but not mode 1. Along-beam phase increase can be used to calculate wavelength and phase velocity (Zhao 2017b). The SSH amplitude can be converted to energy and energy flux (Zhao et al. 2016; Zhao 2018). Along-beam energy decay can be used to track their propagation and dissipation.

Figure 10a shows that the southbound mode-1 waves from Mendocino Ridge can travel at least 2000 km (outside our study region). In contrast, the mode-2 waves are observed to travel about 800 km (Fig. 10b) and the mode-3 waves travel 300 km (Fig. 10c). It suggests that the propagation distance decreases with increasing mode number. The mode-1 waves encounter Fieberling Seamount at 32.3°N. But they are not obviously affected by the isolated seamount. Previous in situ measurements show that Fieberling Seamount has energetic internal wave motions (Kunze and Toole 1997). The MITgcm simulation agrees with in situ measurements, showing that Fieberling Seamount is in the path of the southbound mode-1 waves and generates mode-2 and mode-3 waves itself. Both Figs. 8 and 10 show that the mode-1 internal tidal waves are not affected by isolated seamounts, likely because the internal tide wavelengths are large and seamounts are relatively short. As shown in Fig. 8, there are numerous internal tidal beams of all three modes in the decomposed components. Following each internal tidal beam, we can study their generation, propagation, and decay. A comprehensive investigation of these beams is beyond the scope of this paper.

6. Summary

In this paper, we have presented a decomposition technique to resolve the multimodal multidirectional M_2 internal tide field simulated by the MITgcm. By this technique, different baroclinic modes are decomposed by 2D spatial filtering, and waves of different horizontal propagation directions are decomposed by 2D plane wave analysis. Parameters used in the decomposition are from theoretical values that are calculated using the *World Ocean Atlas 2013*. We applied this technique to the M_2 internal tide field off the U.S. West Coast over the range 20°–50°N, 220°–245°E. We obtained the lowest three baroclinic modes and further decomposed each mode into five waves of arbitrary propagation directions. In the end, the raw M_2 internal tide field was decomposed into 14 components. The sum of the decomposed components approximately yields the raw internal tide field. The internal tidal beams have smooth amplitudes and linear-increasing phases. They are associated with notable topographic features. The overall RMS error in the decomposition technique is 1.43 mm, much lower than the internal tide signal with an amplitude of about 10 mm. All these features validate our decomposition technique.

In this paper, we have demonstrated that the decomposed components reveal unprecedented features, which cannot be observed in the raw multiwave field. There are numerous mode-1, mode-2, and mode-3 internal tidal beams in the decomposed components. For each beam, we showed that we can track the internal tide's generation, propagation, and dissipation with great details. We showed that the mode-1, mode-2, and mode-3 M_2 internal tide fields have very different spatial patterns. The mode-1 waves in the study region are dominantly generated at the Hawaiian Ridge. They are also locally generated at the Mendocino Ridge and continental slope. While the mode-2 and mode-3 waves are generated locally at the Mendocino Ridge, isolated seamounts, and continental slope, the Mendocino Ridge radiates both southbound and northbound internal tidal waves of all three modes. The southbound mode-1 waves may travel over 2000 km. In contrast, the mode-2 and mode-3 waves are tracked for about 800 and 300 km, respectively. We also found that the mode-1 waves are not significantly affected by relatively small seamounts. The results suggest that our decomposition technique is useful to understand and simulate the internal tide field.

7. Discussion

Our decomposition technique can be extended to other tidal constituents and to the global ocean. Using the year-long MITgcm hourly output from September 2011 to November 2012, each tidal constituent can be extracted by pointwise harmonic analysis. Using our decomposition technique, we can further decompose each tidal constituent into a series of components. It is also interesting to compare the decomposed MITgcm internal tides with satellite observations. Previously, the mode-1 and mode-2 M_2 internal tides in this region have been observed using 25 years of satellite altimeter data (Fig. 11 in Zhao 2018). The MITgcm-simulated and satellite-observed internal tide fields have similarities and differences. Both show mode-1 and mode-2 M_2 internal tide radiation from the Mendocino Ridge. However, the internal tide generation at fracture zones is observed by satellite altimetry but not simulated by the MITgcm. It is expected that the comparison may improve

the parameterization and performance of the MITgcm. Since both the satellite-observed and MITgcm-simulated fields have been decomposed into multiple components, we can compare them mode by mode and beam by beam.

This paper demonstrates that our decomposition technique works well on the MITgcm-simulated M_2 internal tide field, which contains little nontidal noise, because it is extracted from hourly model output by harmonic analysis. It might be a challenge to apply this technique to real SSH measurements made by nadir-looking conventional and wide-swath SWOT altimetry. The altimetric measurements contain considerable nontidal noise from a variety of ocean processes. Also, the altimetric measurements have irregular spatiotemporal sampling patterns. Therefore, it is more difficult to extract and decompose the internal tide field from satellite altimetric measurements. We are currently applying this technique to one year of SWOT simulator data, which is obtained by resampling the MITgcm-simulated ocean state (including various ocean dynamic processes) using the SWOT orbiting configuration. We are also applying this technique to existing nadir-looking altimeter data to get decomposed internal tides on a global scale.

Acknowledgments. ZZ was supported by the National Aeronautics and Space Administration (NASA) via NNX17AH14G and NNX17AH57G and the National Science Foundation (NSF) via OCE1634041. JW, DM, and LF were supported by the NASA SWOT mission. SC and BQ were supported by the NASA Project NNX16AH66G. We thank Eric Lindstrom and Eric D'Asaro for their inspiring suggestions. This paper was greatly improved with suggestions from three anonymous reviewers. The MITgcm output analysis for this paper was carried out at the Jet Propulsion Laboratory, California Institute of Technology, under a contract with the National Aeronautics and Space Administration. The *World Ocean Atlas 2013* is produced and made available by NOAA National Oceanographic Data Center (https://www.nodc.noaa.gov/OC5/woa13/). The MITgcm simulation and the decomposed internal tides presented in this paper are available upon request (zzhao@apl.uw.edu).

REFERENCES

Alford, M. H., 2010: Sustained, full-water-column observations of internal waves and mixing near Mendocino Escarpment. *J. Phys. Oceanogr.*, **40**, 2643–2660, https://doi.org/10.1175/2010JPO4502.1.

Althaus, A. M., E. Kunze, and T. B. Sanford, 2003: Internal tide radiation from Mendocino Escarpment. *J. Phys. Oceanogr.*, **33**, 1510–1527, https://doi.org/10.1175/1520-0485(2003)033<1510:ITRFME>2.0.CO;2.

Arbic, B. K., A. J. Wallcraft, and E. J. Metzger, 2010: Concurrent simulation of the eddying general circulation and tides in a global ocean model. *Ocean Modell.*, **32**, 175–187, https://doi.org/10.1016/j.ocemod.2010.01.007.

Buijsman, M. C., B. K. Arbic, J. G. Richman, J. F. Shriver, A. J. Wallcraft, and L. Zamudio, 2017: Semidiurnal internal tide incoherence in the equatorial Pacific. *J. Geophys. Res. Oceans*, **122**, 5286–5305, https://doi.org/10.1002/2016JC012590.

Egbert, G. D., and R. D. Ray, 2000: Significant dissipation of tidal energy in the deep ocean inferred from satellite altimeter data. *Nature*, **405**, 775–778, https://doi.org/10.1038/35015531.

——, and ——, 2001: Estimates of M2 tidal energy dissipation from TOPEX/Poseidon altimeter data. *J. Geophys. Res.*, **106**, 22 475–22 502, https://doi.org/10.1029/2000JC000699.

Fu, L.-L., and C. Ubelmann, 2014: On the transition from profile altimeter to swath altimeter for observing global ocean surface topography. *J. Atmos. Oceanic Technol.*, **31**, 560–568, https://doi.org/10.1175/JTECH-D-13-00109.1.

Garrett, C., and E. Kunze, 2007: Internal tide generation in the deep ocean. *Annu. Rev. Fluid Mech.*, **39**, 57–87, https://doi.org/10.1146/annurev.fluid.39.050905.110227.

Kelly, S. M., J. D. Nash, K. I. Martini, M. H. Alford, and E. Kunze, 2012: The cascade of tidal energy from low to high modes on a continental slope. *J. Phys. Oceanogr.*, **42**, 1217–1232, https://doi.org/10.1175/JPO-D-11-0231.1.

——, N. L. Jones, and J. D. Nash, 2013: A coupled model for Laplace's tidal equations in a fluid with one horizontal dimension and variable depth. *J. Phys. Oceanogr.*, **43**, 1780–1797, https://doi.org/10.1175/JPO-D-12-0147.1.

Kunze, E., and J. M. Toole, 1997: Tidally driven vorticity, diurnal shear, and turbulence atop Fieberling Seamount. *J. Phys. Oceanogr.*, **27**, 2663–2693, https://doi.org/10.1175/1520-0485(1997)027<2663:TDVDSA>2.0.CO;2.

Large, W. G., and S. G. Yeager, 2004: Diurnal to decadal global forcing for ocean and sea-ice models: The datasets and flux climatologies. NCAR Tech. Note TN-460+STR, 105 pp., https://doi.org/10.5065/D6KK98Q6.

Li, Z., J.-S. von Storch, and M. Müller, 2015: The M_2 internal tide simulated by a 1/10° OGCM. *J. Phys. Oceanogr.*, **45**, 3119–3135, https://doi.org/10.1175/JPO-D-14-0228.1.

Locarnini, R. A., and Coauthors, 2013: *Temperature.* Vol. 1, *World Ocean Atlas 2013*, NOAA Atlas NESDIS 73, 40 pp., http://data.nodc.noaa.gov/woa/WOA13/DOC/woa13_vol1.pdf.

Marshall, J., A. Adcroft, C. Hill, L. Perelman, and C. Heisey, 1997: A finite-volume, incompressible Navier Stokes model for studies of the ocean on parallel computers. *J. Geophys. Res.*, **102**, 5753–5766, https://doi.org/10.1029/96JC02775.

Munk, W. H., 1981: Internal waves and small-scale processes. *Evolution of Physical Oceanography*, B. A. Warren and C. Wunsch, Eds., MIT Press, 264–291.

Musgrave, R. C., J. A. MacKinnon, R. Pinkel, A. F. Waterhouse, J. Nash, and S. M. Kelly, 2017: The influence of subinertial internal tides on near-topographic turbulence at the Mendocino Ridge: Observations and modeling. *J. Phys. Oceanogr.*, **47**, 2139–2154, https://doi.org/10.1175/JPO-D-16-0278.1.

Pawlowicz, R., B. Beardsley, and S. Lentz, 2002: Classical tidal harmonic analysis including error estimates in MATLAB using T_TIDE. *Comput. Geosci.*, **28**, 929–937, https://doi.org/10.1016/S0098-3004(02)00013-4.

Ponte, A. L., and P. Klein, 2015: Incoherent signature of internal tides on sea level in idealized numerical simulations. *Geophys. Res. Lett.*, **42**, 1520–1526, https://doi.org/10.1002/2014GL062583.

Qiu, B., S. Chen, P. Klein, J. Wang, H. Torres, L.-L. Fu, and D. Menemenlis, 2018: Seasonality in transition scale from balanced to unbalanced motions in the World Ocean. *J. Phys. Oceanogr.*, **48**, 591–605, https://doi.org/10.1175/JPO-D-17-0169.1.

Rainville, L., and R. Pinkel, 2006: Propagation of low-mode internal waves through the ocean. *J. Phys. Oceanogr.*, **36**, 1220–1236, https://doi.org/10.1175/JPO2889.1.

Ray, R. D., and E. Zaron, 2016: M_2 internal tides and their observed wavenumber spectra from satellite altimetry. *J. Phys. Oceanogr.*, **46**, 3–22, https://doi.org/10.1175/JPO-D-15-0065.1.

Rocha, C. B., T. K. Chereskin, S. T. Gille, and D. Menemenlis, 2016a: Mesoscale to submesoscale wavenumber spectra in Drake Passage. *J. Phys. Oceanogr.*, **46**, 601–620, https://doi.org/10.1175/JPO-D-15-0087.1.

——, S. T. Gille, T. K. Chereskin, and D. Menemenlis, 2016b: Seasonality of submesoscale dynamics in the Kuroshio Extension. *Geophys. Res. Lett.*, **43**, 11 304–11 311, https://doi.org/10.1002/2016GL071349.

Savage, A. C., and Coauthors, 2017: Spectral decomposition of internal gravity wave sea surface height in global models. *J. Geophys. Res. Oceans*, **122**, 7803–7821, https://doi.org/10.1002/2017JC013009.

Su, Z., J. Wang, P. Klein, A. F. Thompson, and D. Menemenlis, 2018: Ocean submesoscales as a key component of the global heat budget. *Nat. Commun.*, **5**, 775, https://doi.org/10.1038/s41467-018-02983-w.

Torres, H. S., P. Klein, D. Menemenlis, B. Qiu, Z. Su, J. Wang, S. Chen, and L.-L. Fu, 2018: Partitioning ocean motions into balanced motions and internal gravity waves: A modeling study in anticipation of future space missions. *J. Geophys. Res. Oceans*, **123**, 8084–8105, https://doi.org/10.1029/2018JC014438.

Wang, J., L.-L. Fu, B. Qiu, D. Menemenlis, J. T. Farrar, Y. Chao, A. F. Thompson, and M. M. Flexas, 2018: An observing system simulation experiment for the calibration and validation of the surface water ocean topography sea surface height measurement using in situ platforms. *J. Atmos. Oceanic Technol.*, **35**, 281–297, https://doi.org/10.1175/JTECH-D-17-0076.1.

Wunsch, C., 1975: Internal tides in the ocean. *Rev. Geophys. Space Phys.*, **13**, 167–182, https://doi.org/10.1029/RG013i001p00167.

——, 2013: Baroclinic motions and energetics as measured by altimeters. *J. Atmos. Oceanic Technol.*, **30**, 140–150, https://doi.org/10.1175/JTECH-D-12-00035.1.

Zaron, E. D., 2019: Baroclinic tidal sea level from exact-repeating mission altimetry. *J. Phys. Oceanogr.*, **49**, 193–210, https://doi.org/10.1175/JPO-D-18-0127.1.

Zhao, Z., 2014: Internal tide radiation from the Luzon Strait. *J. Geophys. Res. Oceans*, **119**, 5434–5448, https://doi.org/10.1002/2014JC010014.

——, 2016: Using CryoSat-2 altimeter data to evaluate M_2 internal tides observed from multisatellite altimetry. *J. Geophys. Res. Oceans*, **121**, 5164–5180, https://doi.org/10.1002/2016JC011805.

——, 2017a: The global mode-1 S_2 internal tide. *J. Geophys. Res. Oceans*, **122**, 8794–8812, https://doi.org/10.1002/2017JC013112.

——, 2017b: Propagation of the semidiurnal internal tide: Phase velocity versus group velocity. *Geophys. Res. Lett.*, **44**, 11 942–11 950, https://doi.org/10.1002/2017GL076008.

——, 2018: The global mode-2 M_2 internal tides. *J. Geophys. Res. Oceans*, **123**, 7725–7746, https://doi.org/10.1029/2018JC014475.

——, M. H. Alford, J. B. Girton, L. Rainville, and H. L. Simmons, 2016: Global observations of open-ocean mode-1 M_2 internal tides. *J. Phys. Oceanogr.*, **46**, 1657–1684, https://doi.org/10.1175/JPO-D-15-0105.1.

Zweng, M., and Coauthors, 2013: *Salinity*. Vol. 2, *World Ocean Atlas 2013*, NOAA Atlas NESDIS 74, 39 pp., http://data.nodc.noaa.gov/woa/WOA13/DOC/woa13_vol2.pdf.